# Analysis and Prevention of Coupling-Dependent Data Flipping in Wireless Power Transfer Systems

Yuan Yao, *Student Member, IEEE*, Sayan Sarkar, *Student Member, IEEE*, Wing-Hung Ki, *Member, IEEE*, and Chi-Ying Tsui, *Senior Member, IEEE*

***Abstract*—Load shift keying (LSK) is widely used in a wireless power transfer (WPT) system to backscatter secondary side information to the primary side. However, when the coupling coefficient ($k$) between the transmitter and the receiver coils is lower than a critical value ($k_{\mathrm{DF}}$), the demodulated LSK data may flip from "1" to "0" or "0" to "1," which is popularly known as coupling-dependent data flipping (CDDF). In this article, the conditions leading to CDDF are analyzed. Parasitic components of the inductive link are included, and both matched and unmatched coupled resonators are analyzed and verified by *SPICE* simulations. An automatic carrier-frequency modulation scheme is proposed to prevent CDDF and is verified by measurement results.**

***Index Terms*—Coupling-dependent data flipping (CDDF), load shift keying (LSK), wireless power transfer (WPT).**

## I. Introduction

WIRELESS power transfer (WPT) techniques based on *LC* resonance have found widespread applications in electric vehicles [1], [2], Internet of Things (IoT) [3], and implantable medical devices (IMDs) [4], [5]. In these techniques, the power amplifier (PA) of the transmitter (*TX*) delivers alternating current (ac) to the primary *LC* tank, and the secondary *LC* tank of the receiver (*RX*) captures the ac magnetic fluxes. A rectifier and a voltage regulator then provide a regulated dc voltage $V_{\mathrm{out}}$ to power up the load on the secondary side. However, during WPT, changes in the loading current of the receiver and the coupling coefficient ($k$) between the primary and secondary coils can affect the output voltage of the receiver ($V_{\mathrm{out}}$). Uplink communication from the *RX* side to the *TX* side can be used to maintain a steady $V_{\mathrm{out}}$ [6], [7], [8]. It is also essential to report the status of the secondary side to the *TX* side, and this communication should be robust against misalignments and interference [9], [10], [11]. One popular scheme involves using different pairs of coils for transferring power and data separately [12], [13], but the cost and size will increase due to the additional coil. Moreover, there may be crosstalk among the coils. In [14], crosstalk is reduced by placing the power coil and the data coil orthogonally, but this requires larger coil sizes. In [15], it is shown that coplanar geometry performs better than orthogonal geometry by separating the pairs of coils for power transfer, downlink data transfer, and uplink data transfer. However, using three pairs of coils increases the area of the inductive link significantly.

One economical way of transferring both power and data is to use only one pair of coils. Wideband frequency-shift keying (FSK) was proposed in [16] to transfer data and power simultaneously, but it requires multiple signal sources operating at different frequencies, resulting in increased power consumption and circuitry complexity. Therefore, FSK is typically used for downlink data telemetry. Cyclic ON-OFF keying [17] and passive phase shift keying [18] were proposed to improve data rate and maintain power transfer efficiency (PTE) during communication. However, both require precise timing control, which adds to the cost of the system.

For applications that do not need a high bandwidth uplink, such as IMDs and RFID tags, load shift keying (LSK) has been widely used because of its simple circuit architecture, low power consumption, and small area requirements [19], [20], [21]. LSK uses a shorting switch (SW) connected in parallel across the load resistance on the *RX* side to modulate the equivalent impedance on the *TX* side by switching SW ON and OFF. The uplink signal can be demodulated by monitoring the input current of or the voltage across the inductor $L_1$ on the *TX* side. Recently, a problem called coupling-dependent data flipping (CDDF) has been reported [22]. The uplink data will be incorrectly demodulated when $k$ is lower than a critical value $k_{\mathrm{DF}}$. In [22], CDDF was analyzed, and the remedy proposed is to monitor the input current of $L_1$ to correctly demodulate the uplink data within the stipulated operating range of $k$. However, in [22], both the *TX* and *RX* resonant tanks were required to be perfectly matched, which is challenging to achieve in practice due to variations in parasitic capacitance of secondary coil caused by changes in environment, especially for IMDs applications [23], [24]. Moreover, in [22], parasitic resistances of inductors were not accounted for, which affects the accuracy of the mathematical analysis.

The major contributions of this article are summarized as follow.

1) We demonstrate through theoretical analysis, simulation, and measurement results that the CDDF prevention

Manuscript received 3 January 2023; revised 7 April 2023; accepted 3 May 2023. Date of publication 11 May 2023; date of current version 21 June 2023. This work was supported by the Hong Kong Innovation and Technology Fund under Grants ITS/015/19 and ITS/023/21. Recommended for publication by Associate Editor J. Acero. *(Corresponding author: Yuan Yao.)*

The authors are with the Department of Electronic and Computer Engineering, The Hong Kong University of Science and Technology, Hong Kong (e-mail: yyaoah@connect.ust.hk; ssarkar@connect.ust.hk; eeki@ust.hk; eetsui@ust.hk).

Color versions of one or more figures in this article are available at https://doi.org/10.1109/TPEL.2023.3275377.

Digital Object Identifier 10.1109/TPEL.2023.3275377

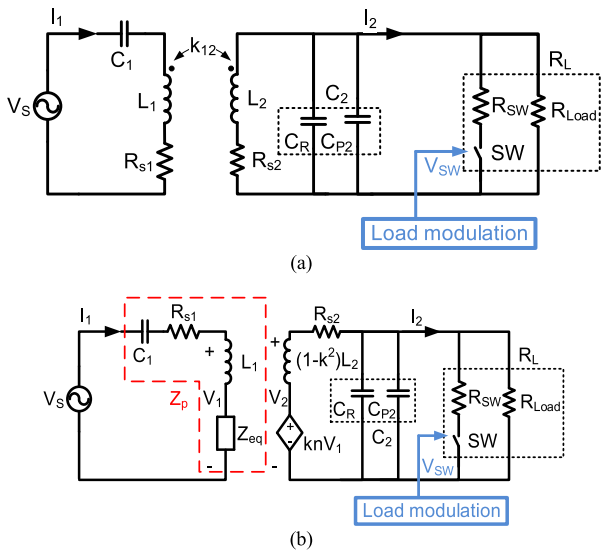


Fig. 1. (a) Simplified block diagram of IMDs. (b) Reflected impedance model.

method proposed in [22] is not applicable for mismatched *LC* tanks.

2) A more comprehensive analysis was presented by taking parasitic parameters into consideration. Based on the analysis, an automatic carrier-frequency modulation scheme is proposed to prevent the LSK signal flipping issue.
3) The proposed scheme is implemented, and the performance is verified through measurement results.

The rest of this article is organized as follows. In Section II, a detailed analysis of a WPT system with SP compensation topology is presented. In Section III, a method of eliminating CDDF is proposed and verified. Implementation of a WPT system that is free from CDDF is described in Section IV and measurement results are presented in Section V. Finally, conclusion is given in Section VI.

## II. Analysis of Coupling-Dependent Data Flipping

### A. Ideal LSK Modulation Scheme

IMDs are low-power applications that typically use a pair of coupled series-parallel resonant coils (*S–P* coils) as the standard implementation. Fig. 1(a) shows the equivalent circuit of a WPT system with *S–P* resonance. Based on the reflected impedance model [25], the equivalent circuit could be transformed to Fig. 1(b). Backscattering of signals from the secondary receiver is detected through monitoring the change in the primary current $I_1$ that is given by

$$I_1\ (s) = \frac{V_s}{Z_p} = \frac{V_s}{Z_1 + Z_{\text{eq}}} \tag{1}$$

where $Z_1$ is the impedance of the primary side and $Z_{\text{eq}}$ is the equivalent reflected impedance from the secondary side. Hence, $Z_p$ is the total primary impedance that accounts for the secondary loading. The impedance of the series $L_1C_1$ tank including the primary parasitic resistance $R_{s1}$ is given by

$$Z_1\left(j\omega\right) = R_{s1} + j\omega L_1 + \frac{1}{j\omega C_1} = R_{s1}\ + jX_1. \tag{2}$$

The primary tank resonance frequency is

$$\omega_{o1} = 2\pi f_{o1} = \frac{1}{\sqrt{L_1C_1}}. \tag{3}$$

On the secondary side, the rectifier load is modeled as an equivalent load resistor $R_L$. When reflected to the primary side, the impedance of the secondary $L_2C_2$ parallel tank is $Z_{\text{eq}}$(s), and is equal to shown at the bottom of this page

$$Z_{eq}(j\omega) = \frac{\omega^2M^2}{R_{s2} + j\omega L_2 + (1/j\omega C_2)\,||R_L} \tag{4}$$

where $M$ is the mutual inductance, $R_{s2}$ is the secondary parasitic resistance, and $C_2$ is the equivalent capacitance consisting of the compensation capacitor $C_R$, and the parasitic capacitors due to the rectifier and other peripheral circuits (not shown in Fig. 1), which are lumped into a single value as $C_{p2}$. Hence, $C_2 = C_R + C_{p2}$. Rationalizing the denominator of (4) yield the expression for $Z_{\text{eq}}(j\omega)$ in (5) shown at the bottom of this page. The frequency of the secondary resonant tank that makes $Z_{\text{eq}}$ a real number is given by

$$\omega_{o2} = \sqrt{\frac{1}{L_2C_2} - \frac{1}{C_2^2R_L^2}}. \tag{6}$$

It should be noted that $\omega_{o2}$ is load-dependent and the equivalent load resistance $R_L$ changes when the signal-bit is backscattered. To backscatter a "0," the switch *SW* is closed and the corresponding load $R_{Ls}$ is

$$R_{Ls} = R_{\text{Load}}\,||R_{\text{sw}} \tag{7}$$

where $R_{\text{SW}}$ is a resistor in series with the switch to limit the load current. To backscatter a "1," SW is opened and the corresponding load $R_{Lo}$ is

$$R_{Lo} = R_{\text{Load}} \gg R_{Ls}. \tag{8}$$

It is worth noting that the subscript "*o*" denotes an open-switch, while "*s*" denotes a closed-switch. Furthermore, it can be observed that both $R_{s2} + R_{Lo}$ and $R_{s2} + R_{Ls}$ increase as $R_{\text{Load}}$ increases. If the condition in (6) is satisfied, then $Z_{\text{eq}}(j\omega_{o2})$ becomes a real number, and it can be expressed as

$$Z_{\text{eq}}\left(j\omega_{o2}\right) = R_{\text{eq}} = \frac{\omega_{o2}^2M^2}{R_{s2} + \frac{R_L}{1+\omega_{o2}^2C_2^2R_L^2}}. \tag{9}$$

Moreover, by substituting (6) into (9), we have

$$Z_{\text{eq}}\left(j\omega_{o2}\right) = R_{\text{eq}} = \frac{\left(\frac{1}{L_2C_2} - \frac{1}{C_2^2R_L^2}\right)M^2}{R_{s2} + \frac{L_2}{C_2R_L}}. \tag{10}$$

$$Z_{\text{eq}}\left(j\omega\right) = \omega^2k^2L_1L_2\frac{R_{\text{Load}} + R_{s2} + \omega^2C_2^2R_{\text{Load}}^2R_{s2} - j\omega\left(L_2 - C_2R_{\text{Load}}^2 + \omega^2C_2^2L_2R_{\text{Load}}^2\right)}{\left(R_{\text{Load}} + R_{s2}\right)^2 + \omega^2\left[L_2^2 + R_{\text{Load}}^2C_2\left(R_{s2}^2C_2 - 2L_2\right)\right] + \omega^4L_2^2C_2^2R_{\text{Load}}^2} \tag{5}$$

Clearly, when $R_L$ increases, $R_{\text{eq}}$ increases.

In summary, the equivalent reflected impedance $Z_{\text{eq}}$ increases monotonously with the secondary loading resistance $R_L$. When the receiver sends a "0" by closing the switch SW, $R_L$ decreases from $R_{Lo} = R_{\text{Load}}$ to $R_{Ls} = R_{\text{Load}} \| R_{\text{SW}}$. As a result, $Z_{\text{eq}}$ decreases from $Z_{\text{eq}\,o}$ to $Z_{\text{eq}\,s}$, and $Z_p$ decreases from $Z_{po}$ to $Z_{ps}$, causing an increase in $I_1$. By measuring the amplitude of $I_1$, the primary unit can demodulate the uplink signal.

### B. Mismatching of Secondary $L_2C_2$ Tank

According to [22], if the *LC* tanks of a WPT system are matched such that the voltage source frequency is the same as the resonant frequency with $\omega_o = \omega_{o1} = \omega_{o2}$, the amplitude of the primary current $|I_1|$ increases as $R_L$ decreases, and decreases as $R_L$ increases. Consequently, a higher $|I_1|$ corresponds to a "0", and a lower $|I_1|$ corresponds to a "1," with no data flipping occurring. However, as shown in (6)–(8), the secondary resonant frequency $\omega_{o2}$ is dependent on the load, which is in turn signal-dependent. Therefore, a few problems arise. First, to ensure that the receiver coil presents a real $Z_{\text{eq}} = R_{\text{eq}}$, $C_2$ has to be adjusted according to $R_L$. Second, the secondary receiver consists of I/O pads, over-voltage protection diodes, and a rectifier, all of which introduce parasitic capacitance to the secondary tank. For instance, by using a probe station and an *LCR* meter, the parasitic capacitance of an I/O pad was measured to be approximately 2 pF. To deliver large load current with low conduction loss, the transistors of the rectifier are large. Moreover, parasitic capacitance may vary due to changes in the environment [23], [24]. Third, to improve patient the comfort, a flexible substrate is commonly employed for the implanted receiver, which is built with a printed-circuit secondary coil. Upon implantation, the flexible secondary coil may bend, altering the inductance value [26], [27]. Hence, an $L_2C_2$ tank that is well-compensated before surgery may become detuned after surgery. If the condition in (6) is not satisfied, $Z_{\text{eq}}$ would be complex, i.e.,

$$Z_{\text{eq}}(j\omega) = R_{\text{eq}} + j\,X_{\text{eq}} = \omega^2\,M^2\,(g_{\text{eq}} + jb_{\text{eq}}) \tag{11}$$

$$M = k\sqrt{L_1L_2},\quad g_{\text{eq}} = \frac{R_{\text{eq}}}{\omega^2 M^2},\quad b_{\text{eq}} = \frac{X_{\text{eq}}}{\omega^2 M^2} \tag{12}$$

where $k$ is the coupling coefficient. A common design strategy is to set the input voltage source to switch at a frequency of

$$\omega_o = \frac{1}{\sqrt{L_1C_1}} = \frac{1}{\sqrt{L_2C_2}}. \tag{13}$$

For the secondary receiver, the resonant frequency $\omega_{o2}$ should be close to $\omega_o$ even with the presence of $R_L$. The following approximation holds

$$\omega_{o2} = \frac{1}{\sqrt{L_2C_2}}\sqrt{1 - \frac{L_2}{C_2R_L^2}} = \omega_o\sqrt{1-\delta^2} \tag{14}$$

$$\frac{L_2}{C_2R_L^2} = \delta^2 \ll 1. \tag{15}$$

Substituting (15) into (4), we have

$$Z_{\text{eq}}(j\omega_o) = \frac{\left(1-\delta^2\right)\omega_o^2 M^2}{R_{s2} + \frac{L_2}{C_2R_L} + j\omega_o L_2\delta^2}. \tag{16}$$

As a result, the magnitude of $Z_{\text{eq}}$ increases monotonously with respect to $R_L$. In fact, using the same approximation, it can be concluded that the magnitude of $Z_p$ also increases monotonously with respect to $R_L$.

Since the voltage source $V_s$ maintains a constant amplitude, the primary current $|I_1|$ is smaller when a "1" is backscattered, and $R_L = R_{Lo}$. Conversely, when a "0" is backscattered, $R_L = R_{Ls}$, and $|I_1|$ is larger. To better comprehend the change in $|I_1|$, it is useful to examine the change in $|Z_p|$, that is, $\Delta|Z_p| = |Z_{po}|$–$|Z_{ps}|$. Under normal conditions, $|Z_{po}| > |Z_{ps}|$, and $\Delta|Z_p| > 0$. Data flipping occurs when $|Z_{po}|$ becomes smaller than $|Z_{ps}|$, resulting in $\Delta|Z_p| < 0$. To determine the condition for data flipping, we propose to investigate the difference $|Z_{po}|$–$|Z_{ps}|$, or equivalently and more conveniently, the difference of the square of the magnitudes. We define

$$\Delta|Z_p|^2 = |Z_{po}|^2 - |Z_{ps}|^2. \tag{17}$$

Expanding the terms yields

$$\Delta|Z_p|^2 = (R_{s1} + R_{\text{eqo}})^2 + (X_1 + X_{\text{eqo}})^2 - (R_{s1} + R_{\text{eqs}})^2 - (X_1 + X_{\text{eqs}})^2. \tag{18}$$

Equation (18) can be simplified as

$$\Delta|Z_p|^2 = R_{\text{eqo}}^2 - R_{\text{eqs}}^2 + X_{\text{eqo}}^2 - X_{\text{eqs}}^2 - 2R_{s1}(R_{\text{eqs}} - R_{\text{eqo}}) - 2X_1(X_{\text{eqs}} - X_{\text{eqo}}). \tag{19}$$

The boundary condition for data flipping to occur is when $\Delta|Z_p|^2 = 0$, and using (11), (19) can be reorganized as

$$2R_{s1}(g_{\text{eqs}} - g_{\text{eqo}}) + 2X_1(b_{\text{eqs}} - b_{\text{eqo}}) = \omega_o^2\,k^2L_1L_2\left(g_{\text{eqo}}^2 - g_{\text{eqs}}^2 + b_{\text{eqo}}^2 - b_{\text{eqs}}^2\right). \tag{20}$$

Therefore, the coupling coefficient that data flipping occurs is

$$k_{\text{DF}} = \sqrt{\frac{2R_{s1}(g_{\text{eqs}} - g_{eqo}) + 2X_1(b_{\text{eqs}} - b_{eqo})}{\omega_o^2L_1L_2\left(g_{eqo}^2 - g_{\text{eqs}}^2 + b_{eqo}^2 - b_{\text{eqs}}^2\right)}}. \tag{21}$$

In [22], CDDF is analyzed under the assumption that $R_{s1}$ and $X_1$ are zero, which may not provide accurate prediction. In this article, we not only analyze the condition for CDDF to occur but also propose a design scheme to prevent CDDF from happening. To this end, we analyze $\Delta|Z_p|^2$ in more detail by normalizing (19) as follows:

$$Y = \frac{\Delta|Z_p|^2}{\omega^2M^2} = \alpha k^2 + 2R_{s1}\beta + 2X_1 \tag{22}$$

where

$$\alpha = \omega^2\,L_1L_2\left(g_{eqo}^2 - g_{eqs}^2 + b_{eqo}^2 - b_{eqs}^2\right) \tag{23}$$

$$\beta = g_{eqo} - g_{\text{eqs}} \tag{24}$$

$$\gamma = b_{\text{eqo}} - b_{\text{eqs}}. \tag{25}$$

Transforming the formula of $\Delta|Z_p|^2$ to $Y$ does not affect the null point. By eliminating the common term $(\omega^2M^2)$, the condition leading to CDDF becomes clear. With a matched $L_1C_1$ tank, if $\alpha$ and $\beta$ has the same polarity, it can be ensured that $Y$

remains positive over the entire range of the coupling coefficient ($0 < k < 1$). CDDF occurs if $\alpha$ and $\beta$ have different polarity. To eliminate CDDF, the component $X_1$ is introduced intentionally to make $R_{s1}\,\beta + X_1\gamma$ is homopolar with $\alpha$. This method will be discussed in more detail in Section III.

Assuming the source frequency $f_s$ is the same as the $L_1C_1$ resonant frequency $f_{o1}$, $X_1 = 0$, and (22) is reduced to

$$Y = \alpha k^2 + 2R_{s1}. \tag{26}$$

Our target application is wirelessly powering an implantable biomedical device. The input source frequency $f_s$ is 40.68 MHz. In order to enhance comprehension of the proposed analysis, the measured inductive link parameters are provided as a numerical example. The primary $L_1C_1$ tank resonates at $f_o = 40.68$ MHz, with $L_1 = 1\,\mu$H, $C_1 = 15.3$ pF and $R_{s1} = 2.3\,\Omega$. For the secondary $L_2C_2$ tank, $L_2 = 740$ nH and $R_{s2} = 3.3\Omega$, and $C_2$ is designed as 20.7 pF to ensure that $L_2C_2$ resonates at 40.68 MHz. The load resistance is taken to be $R_{\rm Load} = 20\,\text{k}\Omega$, and the closed-switch resistance is $R_{SW} = 500\,\Omega$.

The calculated values of $Y$ for the given inductive link parameters are shown in Fig. 2(a) based on the analysis proposed by this article. It can be seen from the figure that as long as the resonate frequency of the secondary $LC$ tank $f_{o2}$( $f_{o2} = \omega_{o2}/2\pi$) is close to $f_o$, $Y$ is positive for $k$ ranging from 0 to 1, indicating absence of CDDF, and we denote this range as the communication window. However, as shown on Fig. 2(b), following the analysis presented in [22] and disregarding parasitic resistance results in $Y$ being positive across the entire range of k, regardless of whether the secondary $LC$ tank is matched or not. This behavior is inconsistent with the reality. The values of $\alpha$ and $\beta$ for the given inductive link parameters are shown in Fig. 2(c). Here $\alpha$ is positive even with a mismatched secondary LC tank. According to (26), when $g_{\rm eqo}$ is smaller than $g_{\rm eqs}$, $\beta$ is negative, and the uplink signal will flip. Fig. 2(c) shows that as long as the resonate frequency of the $RX$ $LC$ tank $f_{o2}$ ($f_{o2} = \omega_{o2}/2\pi$) is close to $f_o$, $\beta$ is positive and the uplink signal will not flip. For the given numerical example discussed in Section III, the communication window is from 0.95 $f_o$ to 1.05$f_o$. If $f_{o2}$ shifts by 5% due to parasitic capacitance or bending of the flexible coil, $\beta$ will be negative and introduce two null points to the function of $Y$. In other words, the method proposed in [22] is valid for the ideal condition; but in practice, especially for IMD applications, it is difficult to guarantee $f_{o2}$ matches with $f_s = f_o$ . A different method is needed to improve the robustness of the backward communication.

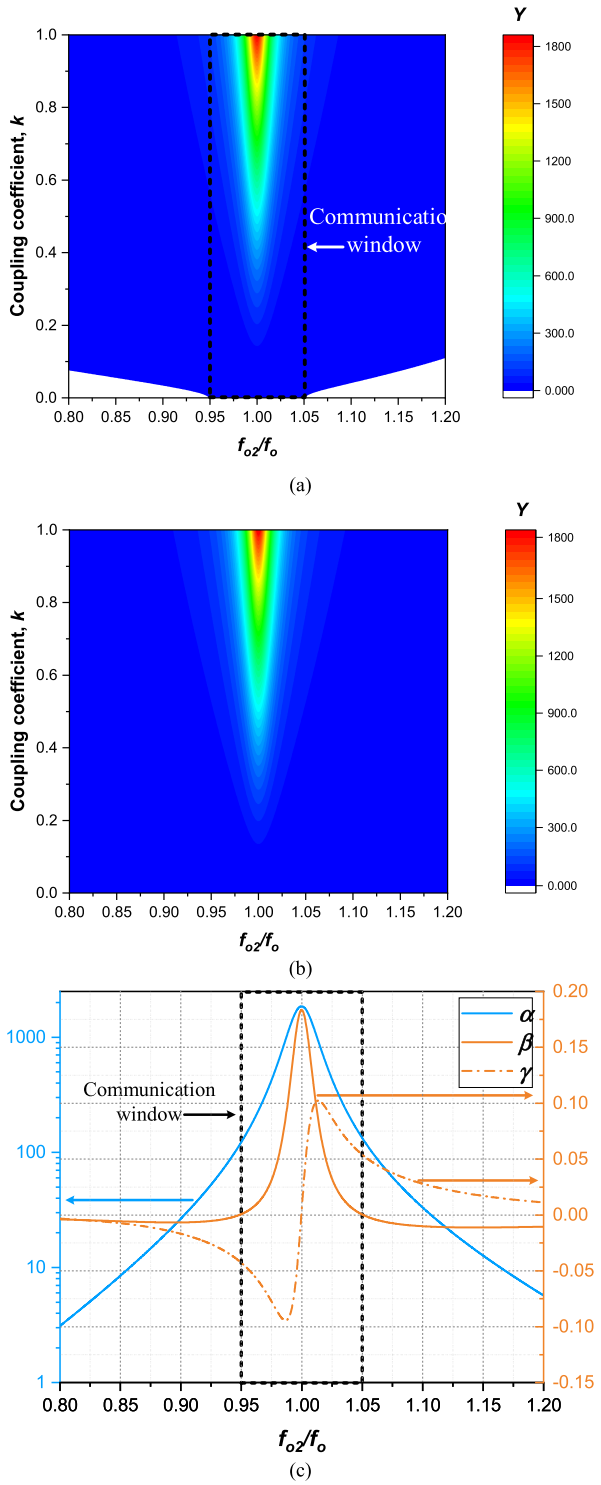


Fig. 2. Calculated values of $Y$ under different values of $k$ and $f_{o2}$ (a) with $R_{s1} = 1\,\Omega$ , (b) with $R_{s1} = 0\,\Omega$, (c) $\alpha$, $\beta$, and $\gamma$ versus $f_{o2}$.

## III. Proposed Method to Prevent CDDF

### A. Circuit Analysis of the Proposed Method

There are three different conditions for the backscattering communication scheme: (1) normal; (2) blackout; and (3) flipping. When $f_s$ is set equal to $f_o$, and $f_{o2}$ is within the communication window, no data flipping occurs, and the LSK scheme is in the normal condition. However, if $f_{o2}$ is outside of the window, then the coupling coefficient $k$ is further examined. If $k \gg k_{\rm DF}$, the LSK scheme is in the normal condition. If $k$ is close to $k_{\rm DF}$, the uplink signal will be too weak to be detected, and the LSK scheme is in the blackout condition. If $k \ll k_{\rm DF}$, then $Y$ becomes negative, indicating that the uplink signal is flipped, resulting in wrong decoded information. One method to prevent data flipping is to implement automatic tuning to adjust the secondary capacitance such that $f_{o2}$ matches well with $f_o$. Autotuning can be achieved through variable-capacitance schemes on the $TX$ and

*RX* sides [28] – [30]. However, variable-capacitance on the *RX* side for high $f_s$ is rarely discussed. For IMD applications, high $f_s$ is preferred for obtaining a better quality factor of the inductor to achieve better PTE with a limited size. In the industrial, scientific, and medical radio bands, 13.56 and 40.68 MHz are commonly chosen for $f_s$ [31] – [33]. Currently, there is no autotuning loop to match $f_{o2}$ for device with 13.56 MHz or higher frequency on the *RX* side because the tuning circuit is required to have higher speed and consume more power.

Another method is to add a known data header at the beginning of the uplink as header bits, such as "010," and then implement an additional demodulator to detect if the uplink signal is flipped. By distinguishing if the detected header bits are flipped (101) or not (010), the uplink signal can be demodulated correctly. However, when the coupling coefficient is equal to $k_{\mathrm{DF}}$, $\Delta|I_1|$ is zero, and the uplink cannot be detected.

In this article, we propose to change the PA switching frequency $f_s$ to modify the value of $X_1$ to prevent CDDF. If the primary *LC* tank no longer satisfies (13), the expression of $Y$ contains an additional component $2X_1\gamma$, and the value of the introduced component $\gamma$ is shown in Fig. 2(c). When $f_{o2}$ is lower than $f_o$, $\gamma$ is negative and to avoid data-flipping, a negative $X_1$ is needed, and vice versa. The flipping issue can be eliminated by ensuring that $X_1\gamma$ satisfies the following:

$$X_1\gamma > -R_{s1}\beta. \tag{27}$$

$Y$ will be positive for the stipulated range of $k$, $(0 < k < 1)$, indicating that data flipping will not occur.

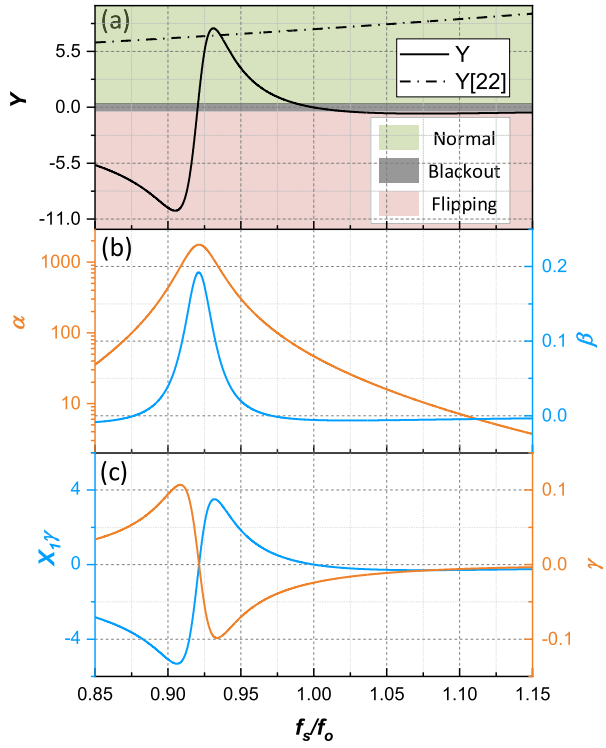


Fig. 3. Calculated values under different switching frequency $f_s$ with mismatched secondary LC tank: (a) the values of *Y*, (b) the values of $\alpha$ and $\beta$, (c) the values of $\gamma$ and $X_1\gamma$.

### B. Analysis and Simulation of Tuning PA Output Frequency

The output frequency $f_s$ of the PA could be adjusted in a few milliseconds, during which the parameters of the *RX* side, such as the bending of the secondary flexible coil can be assumed fixed, and $f_{o2}$ and $k$ are thus constants. The increase of parasitic capacitance due to the presence of saline was measured as $3.7pF$, and the details are discussed in Section V. The based on (22), the values of $Y$ with parasitic capacitors ( $C_{p2} = 3.7pF$) on the *RX* side are calculated and plotted in Fig. 3(a). In order to illustrate the difference between our proposed mathematical analysis and the approach presented in [22], we also calculated the values of *Y* based on the analysis in [22], and labeled the as *Y* [22] in Fig. 3(a). The calculated values of *Y* [22] consistently exhibit positivity, indicating that the LSK scheme operates in normal mode when the switching frequency is varied. It is clear that the previous analysis [22] cannot predict the behavior of the LSK scheme with mismatched *LC* tanks.

When the parasitic capacitor $f_{o2}$ is shifted by 7% from the $L_2C_2$ resonant frequency $f_o$ of (13), and $f_s$ is equal to $f_o$, $\alpha$ is positive while $\beta$ is negative, as shown in Fig. 3(b). In this scenario, when $k$ is smaller then $k_{DF}$, the backscattering scheme is in the flipping condition.

As discussed in Section III-A, reducing $f_s$ is from $f_o$ to a lower frequency results in the primary *LC* tank no longer satisfying (13), and $Y$ contains a component, $2X_1\gamma$. As shown in Fig. 3(c), by reducing $f_s$, $X_1\gamma$ increases initially, causing $Y$ to increase from negative to zero, which means that the uplink signal is immersed in noise, and the system enters the blackout condition. Further reducing $f_s$ increases the value of $Y$ will increase due to the increased $\beta$ and $X_1\gamma$, and the uplink signal can then be detected correctly, and the system enters the normal condition. However, if $f_s$ becomes lower than $f_{o2}$, $\gamma$ changes from negative to positive, while $X_1$ is still negative because $f_s < f_{o1}$, causing $X_1\gamma$ to change from positive to negative. Further reducing $f_s$ causes $Y$ to decrease from positive to negative, and the system will change from normal to flipping. Hence, $f_s$ should be well-controlled to fall between $f_{o2}$ and $f_o$.

For the numerical example given in Section II-B, if there is a $3.7\,pF$ parasitic capacitor on the RX side, the receiver *LC* tank is mismatched ($f_{o2} < f_s$) and the critical coupling coefficient $k_{DF}$ is 0.024. The behavior of LSK scheme was simulated by *SPICE* to verify the calculated value of $k_{\mathrm{DF}}$, and the simulation results are shown in Fig. 4. When $V_{\mathrm{SW}}$ is high, the switch SW is closed, adding $R_{\mathrm{SW}}$ in parallel to the load. For mismatched receiver *LC* tank, if $k$ is larger than $k_{DF}$ , the primary current $I_{1s}$ (when SW is shorted) is larger than $I_{1o}$ (when SW is opened) as shown in Fig. 4(a). At critical coupling ($k = k_{\mathrm{DF}}$) $I_{1s}$ is approximately equal to $I_{1o}$, as shown in Fig. 4(b). If $k$ is smaller than $k_{DF}$, $I_{1s}$ is then lower than $I_{1o}$, and the uplink signal is flipped as shown in Fig. 4(c). The simulation results for the matched $L_2C_2$ tank ($f_{o2} = f_s$) at weak coupling condition ($k < k_{\mathrm{DF}}$) are shown in Fig. 4(d). The uplink signal will not flip as $I_{1s}$ is still larger than $I_{1o}$, indicating that the magnitude of $Z_p$is monotonic with respect to $R_L$. The simulation results are consistent with the theoretical analysis discussed in Section II.

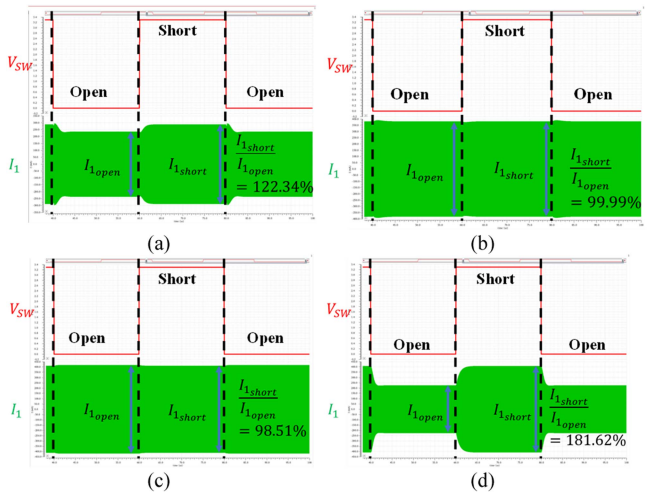


Fig. 4. Simulated waveforms with mismatched LC tank on RX side at (a) $k = 0.044$ ($k > k_{\mathrm{DF}}$). (b) $k = 0.024$ ($k = k_{\mathrm{DF}}$). and (c) $k = 0.015$ ($k < k_{\mathrm{DF}}$). (d) With matched *LC* tank on *RX* side at $k = 0.015$.

TABLE I
RECEIVED HEADER CODE UNDER DIFFERENT CONDITIONS OF BACKSCATTERING SCHEME

| | $uplink$ | $uplink_f$ |
|---|---|---|
| Normal | 010 | 111 |
| Blackout | 111 | 111 |
| Flipping | 111 | 010 |

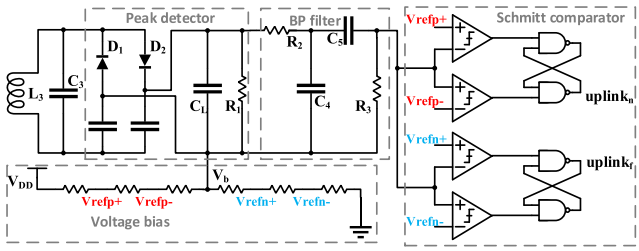


Fig. 6. Data receiver.

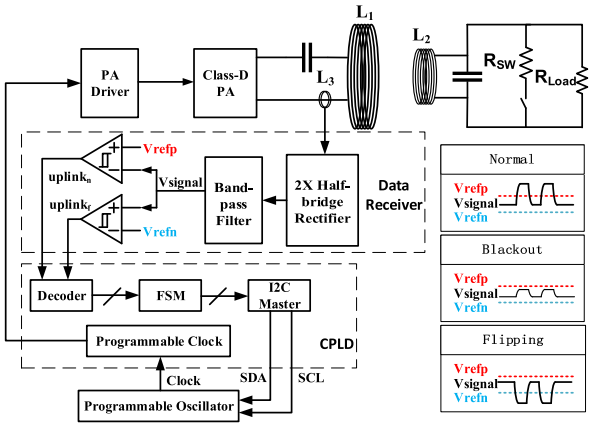


Fig. 5. WPT system diagram with switch frequency autotuning scheme.

## IV. PA SWITCH FREQUENCY AUTOTUNING SCHEME

To prevent data flipping and improve the robustness of the communication link in a WPT system, a PA switching frequency autotuning scheme is implemented. The schematic is shown in Fig. 5. The primary $L_1C_1$ tank is driven by a Class-D PA. The load of the RX side is represented as a resistor $R_{\mathrm{Load}}$. A backscattering switch along with 500 Ω discrete resistor is shunted to $R_{\mathrm{Load}}$. The switch is controlled using a complex programmable logic device (CPLD). Directly sensing the current through the transmitting coil requires a high-performance current sensor integrated with the PA [34], or an additional current probe [22], which increases the system cost and circuit complexity. To address this, a tertiary coil is added to sense the primary current and send the uplink signal to the data receiver, which consists of a peak detector, a band-pass (BP) filter, and two Schmitt trigger comparators. Given that the size limitation is usually more significant on the receiving side and less on the transmitting side, adding a tertiary coil will not pose problem in the implementation. The coupling coefficient between the primary and tertiary coils $k_{13}$ is ten times larger than the coupling coefficient between the secondary and tertiary coils $k_{23}$, ensuring negligible interference from the *RX* side. The peak detector is a 2X half-wave rectifier driving a capacitor and a loading resistor that filters out most of the carrier frequency component. After the BP filter, the filtered data is captured and sent to the Schmitt trigger comparators. The two comparators use different reference voltages to detect the normal and flipping uplink signal, and the demodulated data under different conditions are given in Table I. The uplink data starts with the header bits "010." On the RX side, the switch will turn on to send the "0" bit and turn off to send the "1" bit. If the valid uplink is found in $\mathrm{uplink}_n$, the communication scheme is in normal condition, and if $\mathrm{uplink}_f$ contains the flipped header bits "010", the scheme is in flipping condition. If the header bits are not detected, the system is in blackout condition. The demodulated uplink code will be sent to CPLD, and the conditions of the backscattering scheme will be distinguished by the decoder of the CPLD. A finite state machine (FSM) determines the frequency of the programmable oscillator output, which drives the class-D PA.

The schematic of the data receiver is shown in Fig. 6. $L_3$ is the tertiary coil for sensing $I_1$. The coupling factor with respect to the primary coil $k_{13}$ is constant while the coupling factor with respect to the secondary coil $k_{23}$ is negligible. To stabilize the data receiver, a small capacitor $C_3$ is connected to $L_3$. To prevent excessive power absorption from the primary coil, $C_3$ is chosen such that the resonance frequency of the $L_3C_3$ tank is much higher than the carrier frequency of 40.68 MHz [35]. The half-wave rectifier drives a loading capacitor and a resistor ($C_L$ and $R_1$). A second-order *RC* filter is used to remove dc offset and the coupled noise at the carrier frequency. The bias voltage for the BP filter and the Schmitt trigger comparators are provided by the resistor ladder. By comparing the output of the BP filter $V_{\mathrm{signal}}$ with these reference voltages, the uplink signal is recovered in normal and flipping conditions.

Fig. 7 shows the PA switching frequency control loop state diagram. In previous work [31], the internal circuits sent uplink

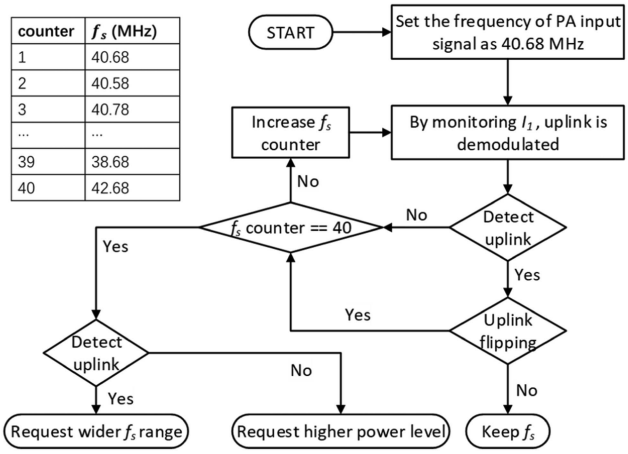


Fig. 7. PA switch frequency control state diagram.

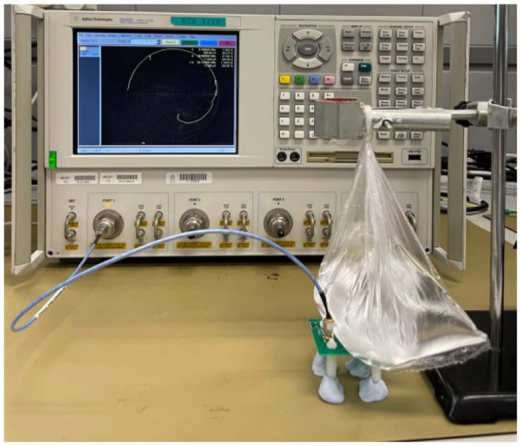

Fig. 8. Experimental setup for measuring resonated frequency of the secondary *LC* tank in the air and saline.

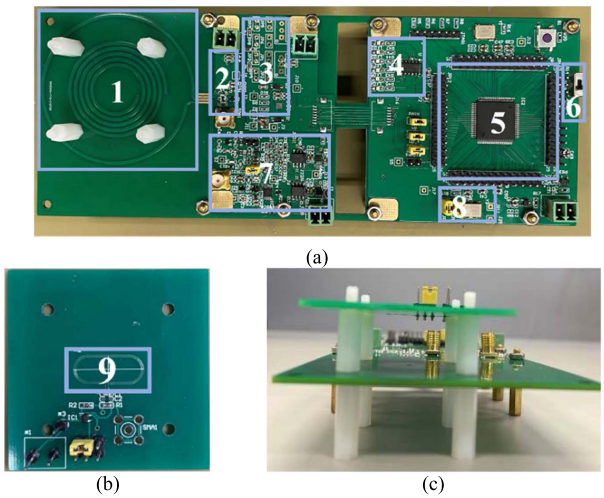


Fig. 9. (a) External system, (b) internal system, and (c) sideview of the WPT system. 1. Primary and detection coil. 2. Class-D PA. 3. PA driver. 4. LED. 5. CPLD core. 6. Autotuning scheme enable button; 7. Programmable oscillator. 8. Data receiver. 9. Secondary coil.

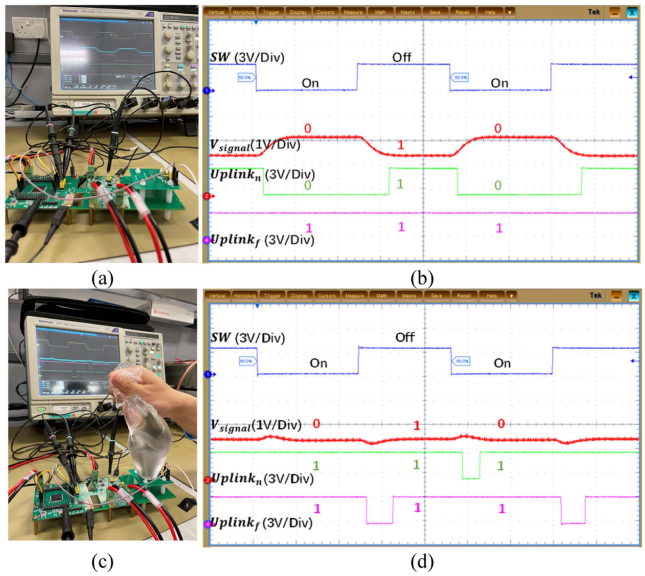


Fig. 10. (a) Experimental setup in air, and (b) the measured waveforms at distance of 20 mm, (c) experimental setup in air and saline, and (d) the measured waveforms at distance of 20 mm.

data to the external unit every 500 $\mu$s. In this article, when the system is power on, the input frequency of PA is set at 40.68 MHz, and the switch SW control signal is generated by CPLD to send uplink data every 500 $\mu$s. A table containing a range of switching frequencies is stored in the CPLD and the $f_s$ modulation step is set at 100 kHz to guarantee that the communication window will not be missed. With a 100 kHz modulation step, it takes 1.2 second to search the entire frequency table. Given that the bending condition, the environment of the receiving coil, and the relative distance between the transmitting and receiving coils typically do not vary rapidly, it is reasonable to assume that $L_2$, $C_2$, and $k$ remain constant during the autotuning period. If a flipping uplink is detected, the CPLD will control the programmable oscillator to sweep the PA driving frequency through $I^2C$ protocol. The settling time for the frequency changes is 10 ms, during which there is no driving signal for the PA, and no uplink data will be received, which is similar to the "blackout" condition. To overcome the "blackout" condition, if the system does not detect the uplink for 20 ms, the CPLD will continue to sweep the switching frequency. The variable frequency range should be able to cover both cases where $f_{o2}$ may be smaller or larger than $f_o$. If a flipped uplink is still detected after sweeping all frequencies in the table, a request signal will be sent out to report that the switching frequency should be further modified to eliminate CDDF. If uplink data is still not detected, a power request bit will be set to "high" to indicate that due to weak coupling, the internal circuits does not receive enough power or the modulation depth is too low to be detected.

## V. Experimental Results

To facilitate measurement, the circuits on the *RX* side are built on a PCB containing the secondary *LC* tank, the switch

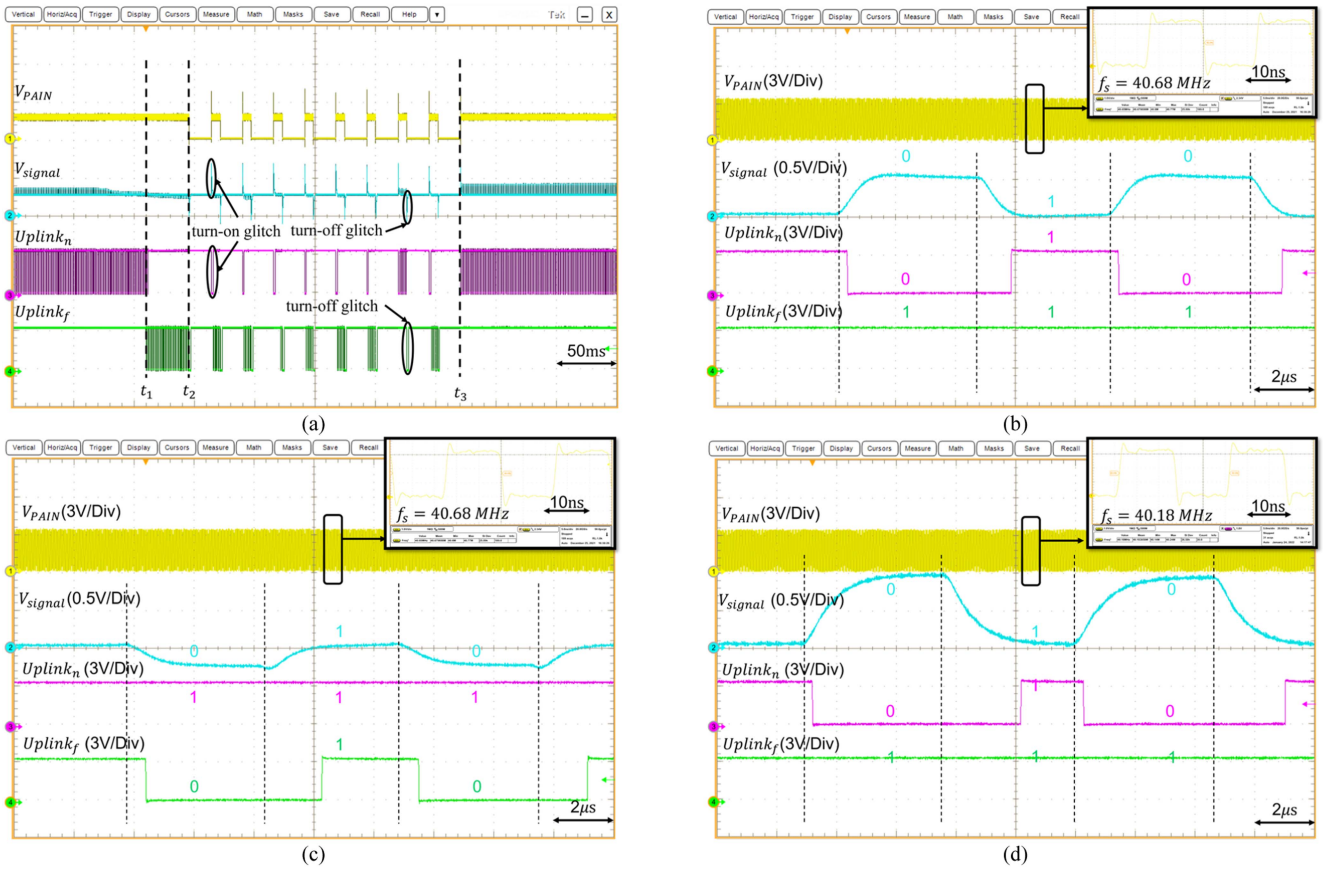


Fig. 11. Measured waveforms (a) during the autotuning procedure, (b) in air, (c) in saline and before tuning $f_s$, and (d) after tuning $f_s$.

TABLE II
MEASURED PARAMETERS OF THE INDUCTIVE LINK

| Parameter | Value | Parameter | Values |
|---|---|---|---|
| $f_o$ | 40.68 MHz | $f_{o2}$ | 40.68 MHz |
| $L_1$ | 1 $\mu$H | $L_2$ | 740 nH |
| $C_1$ | 15.3 pF | $C_2$ | 19.3 pF |
| $R_{s1}$ | 2.3 Ω | $R_{s2}$ | 3.3 Ω |
| $Q_1$ | 111 | $Q_2$ | 57 |

SW, the series resistor $R_{\rm SW}$, and the loading resistor $R_{\rm Load}$. The properties of the inductive link were measured by a vector network analyzer (VNA) and the results are given in Table II. The values of the compensation capacitors are slightly different from the calculated values based on the measured inductance because the discrete capacitor has an accuracy limit of 10%. Fig. 8 shows the measurement setup. The secondary $L_2C_2$ tank was fine-tuned and resonated at 40.68 MHz in the air. To mimic the environment of IMDs [36], [37], a plastic bag (∼10 $\mu$m thick) filled with saline was attached to the surface of the secondary coil, inducing variation in the parasitic capacitance due to environmental effects. The measurements show that the resonant frequency decreases from 40.68 to 37.7 MHz because the parasitic capacitance increases by 3.7 pF due to the presence of saline. After substituting the measured parameters of the inductive link into (21), the value of $k_{DF}$ is determined to be 0.024.

Fig. 9 shows a photograph of the WPT system. The primary and detection coils were fabricated on the same PCB to maintain a constant $k_{13}$. An LED array is used to request a wider range of $f_s$ and higher output power of PA. The relative distance between the primary and secondary coils can be adjusted by tuning the plastic screws.

The values of $k$ at different relative distances were measured using a VNA. The coupling coefficients $k$ are 0.044, 0.025, and 0.015 at distances of 15, 20, and 25 mm, respectively. To demonstrate the effectiveness of the proposed automatic carrier-frequency modulation scheme, the modulation function was disabled, and PA switching frequency was fixed at 40.68 MHz. By setting the distance to 20 mm, the value of $k$ approaches $k_{\rm DF}$. The waveforms of the LSK scheme in different environments are shown in Fig. 10. The testbench in air is shown in Fig. 10(a), and the corresponding waveforms are shown in Fig. 10(b). Since the $LC$ tanks are matched in air, the LSK signal $V_{\rm signal}$ is normal. Fig. 10(c) shows a plastic bag (∼10 $\mu$m thick) filled with saline attached to the surface of the receiving coil to mimic the environment variation. Fig. 10(d) shows that under this setting, $V_{\rm signal}$ is too weak to be detected because $k$ is close to $k_{\rm DF}$ and the LSK scheme is in the blackout condition. The measurement results demonstrate that environment variations can affect the

parasitic capacitor of the secondary coil and subsequently impact the robustness of the LSK scheme. The blackout model predicted by the proposed analysis is verified by the measurement results.

Fig. 11 shows the corresponding waveforms with the environment varying from air to saline to illustrate the effectiveness of the proposed scheme. The secondary $L_2C_2$ tank was well-tuned in air. The distance was adjusted at 25 mm ($k < k_{\mathrm{DF}}$). The waveforms of the automatic tuning control loop in different environments are shown in Fig. 11(a). At $t_1$, a plastic bag ($\sim$10 $\mu$m thick) filled with saline was attached to the surface of the receiving coil, which initially existed in the air. Before $t_1$ the backscattering scheme is in normal condition and $\mathrm{uplink}_n$ contains the header bits as shown in Fig. 11(b). At $t_1$, the environment of the secondary coil changed from air to saline, causing the added parasitic capacitance to lower $f_{o2}$ below $f_s$, and $V_{\mathrm{signal}}$ was reduced instead of increased when the switch *SW* was closed to send "0." As shown in Fig. 11(c), $\mathrm{uplink}_f$ then contains the uplink signal, and the backscattering scheme is in flipping condition. After determining the uplink condition, the FSM then modifies the output frequency of the programmable oscillator accordingly. The oscillator takes 10 ms to settle, during which there is no input signal for the PA potentially introducing turn-ON and turn-OFF glitches. The decoder built in the CPLD filters out the glitches to avoid affecting the detection of the uplink signal. The autotuning scheme takes 230 ms to determine the proper switching frequency. As shown in Fig. 11(d), after $t_3$, the PA input frequency is set as 40.18 MHz, and $V_{\mathrm{signal}}$ increases when the switch SW closes. $\mathrm{uplink}_n$ then contains the uplink signal, and data flipping is prevented.

## VI. Conclusion

In a WPT system with mismatched LC tanks, LSK data can flip in the opposite direction when the coupling coefficient $k$ is smaller than $k_{\mathrm{DF}}$. This problem has been verified by simulation and measurement. A comprehensive analysis of the data flipping issue for a series-parallel compensation topology is presented in this article. Compared to previous studies, the accuracy of the analysis is improved by including parasitic resistance in the analysis. To prevent data flipping, we propose changing the PA switching frequency. A WPT system implementing a PA switching frequency autotuning scheme verifies the existence of data flipping and the effectiveness of the proposed method.

It is worth noting that CDDF occurs independently of the compensation topologies, and the conditions leading to CDDF for other topologies are different and will be analysis in future studies.

## References


[1] F. Corti et al., "A secondary-side controlled electric vehicle wireless charger," *Energies*, vol. 13, no. 24, 2020, Art. no. 6527.

[2] F. Corti, A. Reatti, M. C. Piccirilli, F. Grasso, L. Paolucci, and M. K. Kazimierczuk, "Simultaneous wireless power and data transfer: Overview and application to electric vehicles," in *Proc . IEEE Int. Symp. Circuits Syst.*, Oct. 2020, pp. 1–5.

[3] L. Wang, X. Li, S. Raju, and C. P. Yue, "Simultaneous magnetic resonance wireless power and high-speed data transfer system with cascaded equalizer for variable channel compensation," *IEEE Trans. Power Electron.*, vol. 34, no. 12, pp. 11594–11604, Dec. 2019.

[4] P. Yeon, S. A. Mirbozorgi, J. Lim, and M. Ghovanloo, "Feasibility study on active back telemetry and power transmission through an inductive link for millimeter-sized biomedical implants," *IEEE Trans. Biomed. Circuits Syst.*, vol. 11, no. 6, pp. 1366–1376, Dec. 2017.

[5] G. Wang, W. Liu, M. Sivaprakasam, and G. A. Kendir, "Design and analysis of an adaptive transcutaneous power telemetry for biomedical implants," *IEEE Trans. Circuits Syst. I, Reg. Papers*, vol. 52, no. 10, pp. 2109–2117, Oct. 2005.

[6] R. Shinoda, K. Tomita, Y. Hasegawa, and H. Ishikuro, "Voltage-boosting wireless power delivery system with fast load tracker by $\Delta\Sigma$-modulated sub-harmonic resonant switching," in *Proc. IEEE Int. Solid-State Circuits Conf. Dig. Tech. Papers*, 2012, pp. 288–289.

[7] K. Tomita, R. Shinoda, T. Kuroda, and H. Ishikuro, "1-W 3.3–16.3-V boosting wireless power transfer circuits with vector summing power controller," *IEEE J. Solid State Circuits*, vol. 47, no. 11, pp. 2576–2585, Nov. 2012.

[8] X. Ge, L. Cheng, Y. Yao, and W. H. Ki, "A 6.78 mhz single-stage wireless power transmitter using a 3-mode zero-voltage switching class-D PA," *IEEE Trans. Circuits Syst. I: Regular Papers*, vol. 68, no. 6, pp. 2736–2748, Jun. 2021.

[9] H. Kim, H. Hirayama, S. Kim, K. J. Han, R. Zhang, and J. Choi, "Review of near-field wireless power and communication for biomedical applications," *IEEE Access*, vol. 5, pp. 21264–21285, 2017.

[10] B. Lee and M. Ghovanloo, "An overview of data telemetry in inductively powered implantable biomedical devices," *IEEE Commun. Mag.*, vol. 57, no. 2, pp. 74–80, Feb. 2019.

[11] A. Trigui, S. Hached, A. C. Ammari, Y. Savaria, and M. Sawan, "Maximizing data transmission rate for implantable devices over a single inductive link: Methodological review," *IEEE Rev. Biomed. Eng.*, vol. 12, pp. 72–87, 2018.

[12] G. Wang, P. Wang, Y. Tang, and W. Liu, "Analysis of dual band power and data telemetry for biomedical implants," *IEEE Trans. Biomed. Circuits Syst.*, vol. 6, no. 3, pp. 208–215, Jun. 2012.

[13] L. S. Theogarajan, "A low-power fully implantable 15-channel retinal stimulator chip," *IEEE J. Solid State Circuits*, vol. 43, no. 10, pp. 2322–2337, Oct. 2008.

[14] M. Ghovanloo and S. Atluri, "A wide-band power-efficient inductive wireless link for implantable microelectronic devices using multiple carriers," *IEEE Trans. Circuits Syst. I, Reg. Papers*, vol. 54, no. 10, pp. 2211–2221, Oct. 2007.

[15] G. Simard, M. Sawan, and D. Massicotte, "High-speed OQPSK and efficient power transfer through inductive link for biomedical implants," *IEEE Trans. Biomed. Circuits Syst.*, vol. 4, no. 3, pp. 192–200, Jun. 2010.

[16] M. Ghovanloo and K. Najafi, "A wideband frequency-shift keying wireless link for inductively powered biomedical implants," *IEEE Trans. Circuits Syst. I, Reg. Papers*, vol. 51, no. 12, pp. 2374–2383, Dec. 2004.

[17] S. Ha, C. Kim, J. Park, S. Joshi, and G. Cauwenberghs, "Energy recycling telemetry IC with simultaneous 11.5 mW power and 6.78 mb/s backward data delivery over a single 13.56 mhz inductive link," *IEEE J. Solid State Circuits*, vol. 51, no. 11, pp. 2664–2678, Nov. 2016.

[18] D. Jiang, D. Cirmirakis, M. Schormans, T. A. Perkins, N. Donaldson, and A. Demosthenous, "An integrated passive phase-shift keying modulator for biomedical implants with power telemetry over a single inductive link," *IEEE Trans. Biomed. Circuits Syst.*, vol. 11, no. 1, pp. 64–77, Feb. 2017.

[19] S. Mandal and R. Sarpeshkar, "Power-efficient impedance-modulation wireless data links for biomedical implants," *IEEE Trans. Biomed. Circuits Syst.*, vol. 2, no. 4, pp. 301–315, Dec. 2008.

[20] X. Li, C. Y. Tsui, and W. H. Ki, "A 13.56 mhz wireless power transfer system with reconfigurable resonant regulating rectifier and wireless power control for implantable medical devices," *IEEE J. Solid State Circuits*, vol. 50, no. 4, pp. 978–989, Apr. 2015.

[21] C. Huang, T. Kawajiri, and H. Ishikuro, "A 13.56-mhz wireless power transfer system with enhanced load-transient response and efficiency by fully integrated wireless constant-idle-time control for biomedical implants," *IEEE J. Solid State Circuits*, vol. 53, no. 2, pp. 538–551, Feb. 2017.

[22] H. Qiu, Y. Jiang, Y. Shi, T. Sakurai, and M. Takamiya, "Analysis and mitigation of coupling-dependent data flipping in wireless power and data transfer system," *IEEE Trans. Circuits Syst. I, Reg. Papers*, vol. 68, no. 12, pp. 5182–5193, Dec. 2021.

[23] J. Kim et al., "In vitro and in vivo measurement for biological applications using micromachined probe," *IEEE Trans. Microw. Theory Tech.*, vol. 53, no. 11, pp. 3415–3421, Nov. 2005.

[24] S. Gabriel, R. W. Lau, and C. Gabriel, "The dielectric properties of biological tissues: II. Measurements in the frequency range 10 hz to 20 ghz," *Phys. Med. Biol.*, vol. 41, no. 11, pp. 2251, 1996.

[25] K. Van Schuylenbergh and R. Puers, *Inductive Powering: Basic Theory and Application to Biomedical Systems*. Berlin, Germany: Springer, 2009.
[26] Q. Bai, J. Rigelsford, and R. Langley, "Crumpling of microstrip antenna array," *IEEE Trans. Antennas Propag.*, vol. 61, no. 9, pp. 4567–4576, Sep. 2013.
[27] Y. Yao, X. Meng, C. Y. Tsui, and W. H. Ki, "Polyimide-based flexible 3-coil inductive link design and optimization," in *Proc. IEEE Asia Pac. Conf. Circuits Syst.*, 2018, pp. 505–508.
[28] H. Kennedy, R. Bodnar, T. Lee, and W. Redman-White, "A self-tuning resonant-inductive-link transmit driver using quadrature symmetric delay trimmable phase-switched fractional capacitance," *IEEE J. Solid State Circuits*, vol. 53, no. 6, pp. 1694–1706, 2018.
[29] Y. Lim, H. Tang, S. Lim, and J. Park, "An adaptive impedance-matching network based on a novel capacitor matrix for wireless power transfer," *IEEE Trans. Power Electron.*, vol. 29, no. 8, pp. 4403–4413, Aug. 2014.
[30] Z. Huang, C. Lam, P. Mak, R. P. da Silva Martins, S. Wong, and K. T. Chi, "A single-stage inductive-power-transfer converter for constant-power and maximum-efficiency battery charging," *IEEE Trans. Power Electron.*, vol. 35, no. 9, pp. 8973–8984, Sep. 2020.
[31] X. Li, Y. Lu, X. Meng, C. Y. Tsui, and W. H. Ki, "Optic nerve stimulation system with adaptive wireless powering and data telemetry," *Micromachines*, vol. 8, no. 12, 2017, Art. no. 368.
[32] Y. Lu, X. Li, W. H. Ki, C. Y. Tsui, and C. P. Yue, "A 13.56 mhz fully integrated 1X/2X active rectifier with compensated bias current for inductively powered devices," in *Proc. IEEE Int. Solid-State Circuits Conf. Dig. Tech. Papers*, 2013, pp. 66–67.
[33] W. Liu et al., "A neuro-stimulus chip with telemetry unit for retinal prosthetic device," *IEEE J. Solid State Circuits*, vol. 35, no. 10, pp. 1487–1497, Oct. 2000.
[34] X. Li, X. Meng, C. Tsui, and W. Ki, "Reconfigurable resonant regulating rectifier with primary equalization for extended coupling-and loading-range in bio-implant wireless power transfer," *IEEE Trans. Biomed. Circuits Syst.*, vol. 9, no. 6, pp. 875–884, Dec. 2015.
[35] S. Sarkar, Y. Yao, C. Y. Tsui, and W. H. Ki, "Design strategy of off-resonant tertiary coils for uplink detection in biomedical implants," in *Proc. IEEE Int. Symp. Circuits Syst.*, 2022, pp. 1–5,.
[36] P. J. Rousche, D. S. Pellinen, D. P. Pivin, Jr., J. C. Williams, R. J. Vetter, and D. R. Kipke, "Flexible polyimide-based intracortical electrode arrays with bioactive capability," *IEEE Trans. Biomed. Eng.*, vol. 48, pp. 361–371, Mar. 2001.
[37] S. Hwang et al., "A physically transient form of silicon electronics," *Science*, vol. 337, pp. 1640–1644, Sep. 2012.

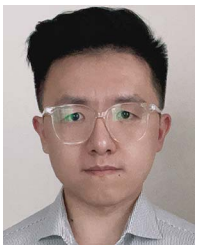

**Yuan Yao** (Student Member, IEEE) received the B.Eng. degree in electronic science and technology from Northeastern University, Shenyang, China, in 2014, and the M.Phil. degree in electronic and computer engineering from The Hong Kong University of Science and Technology, Hong Kong, in 2019, where he is currently working toward the Ph.D. degree with the Department of Electronic and Computer Engineering.

His research interests include near field antenna design, wireless power transfer system design, and implantable medical devices design.

**Sayan Sarkar** (Student Member, IEEE) received the B.Tech degree in electrical engineering from the National Institute of Technology, Durgapur, India, in 2016. Since 2018, he has been working toward the Ph.D. degree with the Department of Electronic and Computer Engineering.

For two years, he was an Assistant manager with Coal India. His research interests include near antenna design, wireless power transfer system design, biomedical instrumentation, and implantable medical device design.

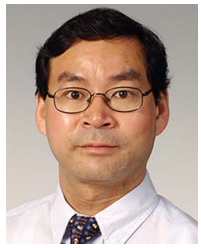

**Wing-Hung Ki** (Member, IEEE) received the B.Sc. degree from the University of California, San Diego, CA, USA, in 1984, the M.Sc. degree from the California Institute of Technology, Pasadena, CA, USA, in 1985, and the Ph.D. degree from the University of California, Los Angeles, CA, USA, in 1995.

He was a Senior Design Engineer with Micro Linear Corporation and then joined The Hong Kong University of Science and Technology, where he is currently a Professor with the Department of Electronic and Computer Engineering. His research interests are power management integrated circuits and systems, which include switch mode power converters, switched-capacitor converters, wireless power transfer transmitters and receivers, and fundamental research in analog integrated circuit analysis and design.

**Chi-Ying Tsui** (Senior Member, IEEE) received the B.S. degree in electrical engineering from the University of Hong Kong, Hong Kong, and the Ph.D. degree in computer engineering from the University of Southern California, Los Angeles, CA, USA, in 1994.

He was with the Department of Electrical and Electronic Engineering, Hong Kong University of Science and Technology, Hong Kong, in 1994 and is a Full Professor with the Department. He is also the Founding Head and a Professor of the Division of Integrative Systems and Design. He has authored or coauthored more than 270 referred publications and holds 14 US patents on power management, VLSI and multimedia systems. His research interests include designing integrated circuits and VLSI architectures for energy-efficient embedded machine learning, low power multimedia, wireless and artificial intelligence applications, developing power management circuits and techniques for embedded portable devices and ultralow power systems.

Dr. Tsui was the recipient of the best paper awards from the IEEE TRANSACTIONS ON VLSI SYSTEMS in 1995, IEEE ISCAS in 1999, ACM/IEEE International Symposium on Low Power Electronics and Designin 2007, and IEEE International Symposium on Electronic Design, Test and Applications in 2008, and International Residential Code for One- and Two-Family Dwelling2012. He was also the recipient of the Design Awards in the IEEE ASP-DAC University Design Contest in 2004 and 2006.